ARTICLES
PUBLISHED ONLINE: 12 SEPTEMBER 2010 | DOI: 10.1038/NPHOTON.2010.204
nature photonics

# Microscopy with self-reconstructing beams

Florian O. Fahrbach[1,2]*, Philipp Simon[2] and Alexander Rohrbach[1,2]*

**Although self-reconstructing beams have been the focus of many scientific studies over the past decade, hardly anything is known about their propagation and self-healing behaviour in a three-dimensional, inhomogeneous medium. The controlled reduction of scattering and beam spreading would enable a new illumination concept for light microscopes, particularly for those designed to look deep into scattering tissue. By investigating three different classes of refractive index inhomogeneity, using two large glass spheres, a cluster of smaller spheres and a piece of human skin, respectively, we show that beam self-reconstruction is indeed possible. We demonstrate that a Bessel beam is unexpectedly robust against deflection at objects, and we define measures for self-reconstruction in this context. We present a prototype of a microscope with self-reconstructing beams (MISERB) and show that a holographically shaped, scanned Bessel beam not only reduces scattering artefacts, but also simultaneously increases image quality and penetration depth in dense media.**

Self-healing of matter and light beams have long been fascinating phenomena in both basic and applied research, also providing inspiration to writers of science fiction. In matter, self-healing is dominated by the highly coupled diffusion of a complex system in a multidimensional landscape of Gibbs free energy, but self-healing of light beams requires the delocalized transport of beam energy and momentum that can replace scattered photons in the centre of the beam.

The idea of self-reconstructing beams originates with work on phase axicons[1,2] and annular pupils[3], resulting in beams with an enhanced depth of field. The Bessel beams generated in this manner were later termed 'non-diffracting beams'[4]. Their intensity profile in free space does not change, because their plane-wave components do not run significantly out of phase in the propagation direction $z$, which would otherwise lead to beam spreading as in normal beams such as Gaussian beams.

Self-healing or self-reconstruction of light beams may occur behind a perturbation of the field by a scatterer, which locally shifts the phase or absorbs energy. It has been shown in simple experiments how a Bessel beam[5] or a vortex beam[6] can recover its initial intensity profile after being obscured by a single obstacle. This work was extended to other non-diffracting beams[7–9], in both continuous-wave (c.w.) and pulsed forms[10,11].

In one notable experiment, a Bessel beam was used to simultaneously manipulate several particles using optical forces[12]. This demonstrated the potential of self-reconstructing beams in future applications in nano- or biotechnology. A few studies have shown that beams can reconstruct, in principle, after propagating through a plane of beads[12] or a suspension of small beads[8]. However, the behaviour of self-reconstructing beams in more complex or even biological materials has not yet been explored.

A major problem in modern microscopy is the scattering of both illumination light and light emitted from the object, which degrades image contrast, particularly in thick media with object sizes larger than ~0.1 mm. In the past, this problem was described by photon diffusion[13], which considers incoherent light propagation from a distribution of point sources. However, modern microscopes use laser-scan techniques, in which coherent illumination and light propagation usually lead to specimen-induced beam aberrations[14]. Coherent light scattering therefore also occurs in point-scanning systems such as confocal or two-photon microscopes, where scattered point intensities are added. Coherent light scattering also becomes more pronounced in line-scanning systems or plane-scanning systems as a result of coherent field superposition. Scattered illumination light can lead to strong image artefacts, resulting in superposition of an uncorrelated ghost image over the ideal image[15].

The effect of ghost images becomes apparent in a light-sheet-based type of microscope, where the illumination lens and the detection lens are arranged at 90° to one another. Illumination

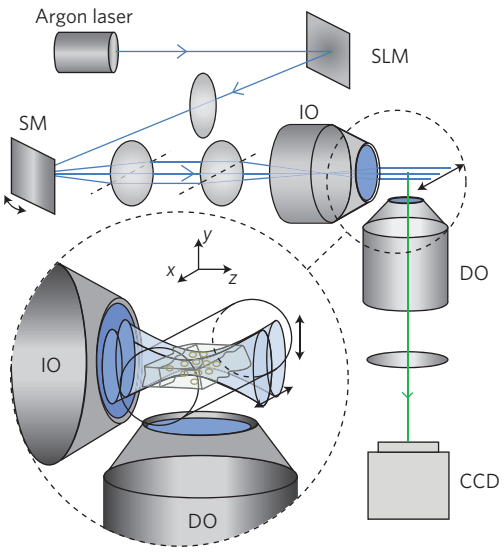


**Figure 1 | Schematic of the set-up.** An argon laser illuminates a spatial light modulator (SLM), which is imaged into the focal plane of the illumination objective (IO) (LD Achroplan 20 × /0.4 Corr, Zeiss). The scan mirrors (SM) enable a beam tilt in the back focal plane of the IO, leading to a lateral scan of the holographically shaped beam in the $x$-direction. In the time average, a light sheet is generated that illuminates only the part of the object in the focal plane of the detection objective (DO) (W-Achroplan 63 × /0.95, Zeiss). Fluorescence light is detected in the orthogonal $y$-direction and imaged onto a CCD camera.

[1]Centre for Biological Signalling Studies (bioss), University of Freiburg, Germany, [2]Laboratory for Bio- and Nano-Photonics, Department of Microsystems Engineering-IMTEK, University of Freiburg, Freiburg 79110, Germany. *e-mail: fahrbach@imtek.de; rohrbach@imtek.de

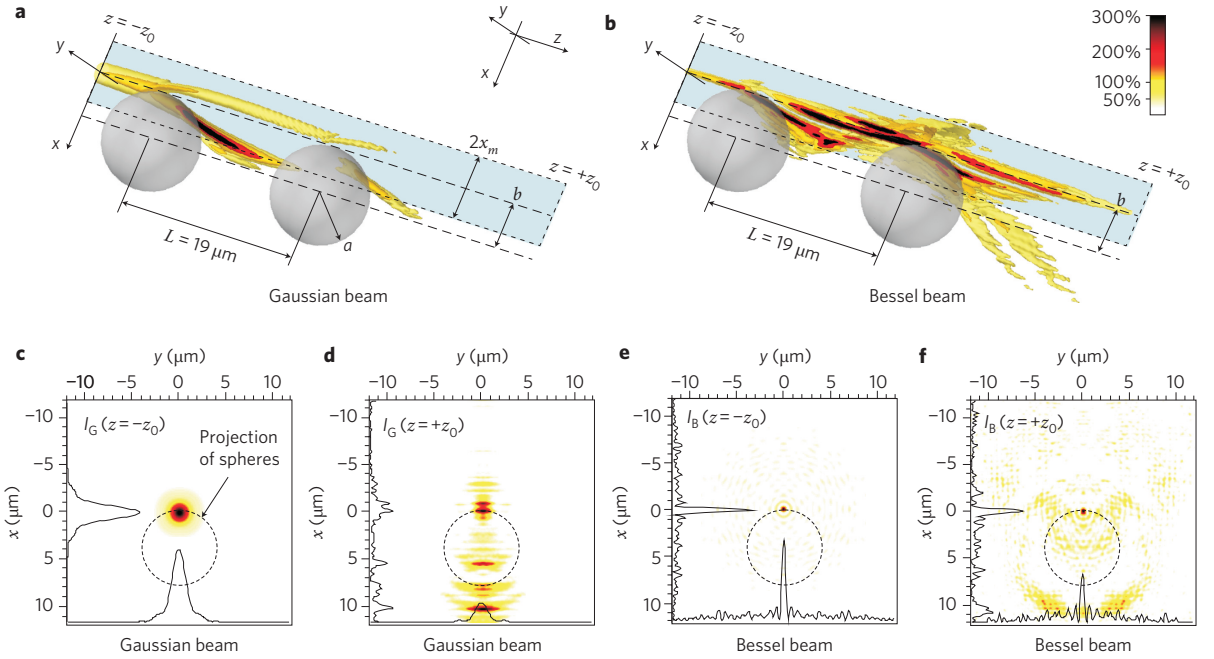


**Figure 2 | Simulation of intensity distributions of Gaussian and Bessel beams scattered by two spheres. a,b**, Intensity isosurfaces at 50%, 100%, 200% and 300% of $I_{max}(z=-z_0)$. The area shaded in light blue indicates the width $2x_m$ over which beam intensities are averaged in Fig. 3. **c**–**f**, Intensity cross-sections $I(x,y,z=-23\,\mu m)$ before (**c**,**e**) and $I(x,y,z=+23\,\mu m)$ behind (**d**,**f**) the two spheres. Linescans through the beam centre quantify beam widths and intensities. The parameters are NA = 0.15 for the Gaussian beam (**a**,**c**,**d**) and NA = 0.3, $\varepsilon = 0.8$ for the Bessel beam (**b**,**e**,**f**). The spheres (radius $a = 4\,\mu m$, $n = 1.41$) are displaced by a distance $b$ (here, $b = a$) from the beam axis in the $x$-direction.

light penetrates the sample from the side and, being focused to a thin light sheet, only excites fluorescence in that part of the object that is in the focal plane of the detection lens. In contrast, in conventional and confocal microscopes many more parts of the object are illuminated (or fluorophores excited) than are detected. Furthermore, a light-sheet-based type of microscope is faster in terms of image acquisition than a point-scanning confocal microscope, because it can be driven in a plane-scanning configuration by using a cylindrical lens[16–19] or in a line-scanning configuration by using a laterally scanned Gaussian beam[20]. Therefore, light-sheet-based microscopes have proven to be very effective for the three- and four-dimensional imaging of large biological specimens[21,22].

In this Article, we illustrate coherent light propagation and scattering through inhomogeneous media by exciting fluorescence in a plane parallel to the propagation axis using a light-sheet-based microscope. We compare beam spreading and deflection of normal and self-reconstructing beams when interacting with different dielectric scatterers, covering three different classes of refractive index inhomogeneity. We identify different measures of self-reconstruction for a modified Bessel beam relative to a focused Gaussian beam. We further show that a scanned Bessel beam generated by a computer hologram can produce high-quality images in strongly scattering media such as human skin.

Our imaging technique is called microscopy with self-reconstructing beams (MISERB) and uses the abovementioned arrangement with an illumination objective (IO) and a detection objective (DO) oriented perpendicular to one another. As in other approaches[19,20], the object is illuminated from the side through the generation of a thin light sheet. However, in our approach we use a computer hologram generated by a spatial light modulator (SLM, HOLOEYE LC-R 2500) (Fig. 1). The modulated Gaussian laser beam ($\lambda = 488$ nm) obtains a special designed phase $\phi_{holo}(x,y)$ to generate a self-reconstructing beam with intensity profile $h_{holo}(\mathbf{r}) = |\mathbf{E}_{holo}(\mathbf{r})|^2$. This beam is designed to excite fluorescence light in the plane of focus of the DO, which is detected in the orthogonal $y$-direction. The object, embedded in a cylinder of fluorescein-stained agarose gel, is then moved along $y$ to obtain a stack of $N$ images $p(x,y_j,z)$ $(j = 1,\ldots,N)$.

However, a real, non-idealized image is obtained by superposition of unscattered illumination laser light and illumination light scattered at the object, with total intensity

$$\begin{aligned} h_{ill}(\mathbf{r}) &= |E_{tot}(\mathbf{r})|^2 = |\mathbf{E}_{holo}(\mathbf{r}) + \mathbf{E}_{sca}(\mathbf{r})|^2 \\ &= |\mathbf{E}_{holo}(\mathbf{r})|^2 + (|\mathbf{E}_{sca}(\mathbf{r})|^2 + 2\mathrm{Re}\{\mathbf{E}^*_{holo}(\mathbf{r}) \cdot \mathbf{E}_{sca}(\mathbf{r})\}) \\ &= h_{holo}(\mathbf{r}) + h_{sca}(\mathbf{r}) \end{aligned} \quad (1)$$

where $\mathbf{E}_{holo}$ and $\mathbf{E}_{sca}$ are the unscattered and scattered fields, respectively. Both intensities $h_{holo}(\mathbf{r})$ and $h_{sca}(\mathbf{r})$ illuminate and excite a fluorophore distribution $C(\mathbf{r})$, which is then detected via a probability distribution $h_{det}(\mathbf{r})$. Therefore, a three-dimensional image $p(\mathbf{r})$ is obtained by a convolution (denoted by *) with the detection point-spread function $h_{det}(\mathbf{r})$ according to[15]

$$p(\mathbf{r}) = ((h_{holo}(\mathbf{r}) + h_{sca}(\mathbf{r})) \cdot C(\mathbf{r}))^* h_{det}(\mathbf{r}) \quad (2)$$

The second term, $h_{sca}(\mathbf{r})$, can become negative, because it contains the interference term and produces artefacts $(h_{sca}(\mathbf{r})\cdot C(\mathbf{r}))^* h_{det}(\mathbf{r})$ in the image. These artefacts increase with $h_{sca}(\mathbf{r})$ and propagation distance $z$ (ref. 15). A clear goal in the development of new microscopy techniques must therefore be the reduction of light scattering inside the sample, which until recently has been considered a hopeless task.

To answer the question as to what extent self-reconstructing beams such as Bessel beams can help to reduce scattering artefacts, one has to define measures for self-reconstruction in inhomogeneous media. Self-reconstructing beams must have the ability to restore their initial intensity profile $h_{holo}(\mathbf{r})$ after interaction with scatterers. This means that the intensity difference $|h_{ill}(\mathbf{r}) - h_{holo}(\mathbf{r})|$ between the unperturbed beam $h_{holo}(\mathbf{r})$ and the beam

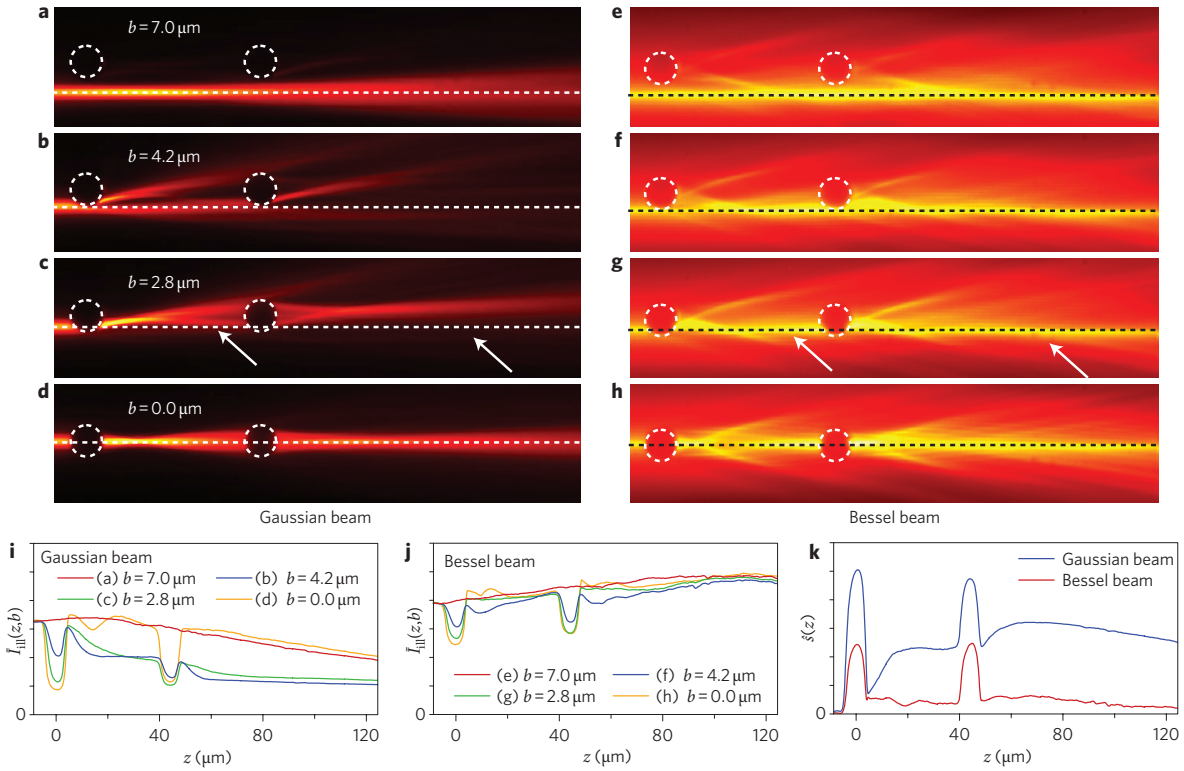


**Figure 3 | Measurement of beam propagation in a fluorescing gel with two large glass spheres arranged consecutively at various beam distances.** **a**–**h**, Images for varying distances $b$ between the spheres and the beam axis for a Gaussian beam (**a**–**d**) and for a Bessel beam (**e**–**h**). The non-fluorescing spheres (diameter $2a = 8\,\mu m$) are outlined by white circles. The white arrows indicate no (**c**) and good (**g**) self-reconstruction behind the scatterers. All images have the same dynamic range. **i**,**j**, Intensity linescans $I_{ill}(z,b)$ along the dashed lines (width $2x_m = 4\,\mu m$) for the Gaussian beam (**i**) and the Bessel beam (**j**). **k**, Standard deviations $\hat{s}(z)$ of $I_{ill}(z,b)$ for each propagation distance $z$.

$h_{ill}(\mathbf{r},\mathbf{b}_i)$ perturbed by any scatterer at positions $\mathbf{b}_i$ must be minimal, such that $|h_{sca}(\mathbf{r},\mathbf{b}_i)| = |h_{ill}(\mathbf{r},\mathbf{b}_i) - h_{holo}(\mathbf{r})| \rightarrow \min$. For a self-reconstructing beam this requirement must be fulfilled for all distances $b = |\mathbf{b}|$ from the scatterer position to the beam axis. The beam position, and therefore $b$, is varied by the scan mirrors. Let $\bar{I}_{ill}(z, b)$ be the intensity $h_{ill}(x,z,b)$ of a beam at position $b$ relative to a scatterer, averaged laterally over a few micrometres. We now can derive the standard deviation $\hat{s}(z)$ or the variance $\hat{s}(z)^2$ between the unperturbed beam intensity $\bar{I}_{holo}(z)$ and the perturbed beam intensity $\bar{I}_{ill}(z, b)$ as a function of the propagation distance $z$:

$$\hat{s}(z)^2 = \frac{1}{\bar{I}_{holo}(z)^2}\int_{-\infty}^{\infty}\left(\bar{I}_{holo}(z) - \bar{I}_{ill}(z,b)\right)^2 \mathrm{d}b \rightarrow \min \qquad (3)$$

To account for the natural beam spread or intensity decay of $\bar{I}_{holo}(z)$ along $z$, that is, a limited beam self-reconstruction in free space, we use a normalized standard deviation $\hat{s}(z) = s(z)/\bar{I}_{holo}(z)$ by dividing by the averaged unperturbed beam intensity. The smaller $\hat{s}(z)$ is for every propagation distance $z$, the smaller is the beam deflection or scattering by a particle. As outlined above, the beam intensities $h_{holo}$ and $h_{ill}$ along $z$ were averaged over a region of width $2x_m$ such that

$$\bar{I}(z) = (2x_m)^{-1}\int_{-x_m}^{x_m} h(x,z)\mathrm{d}x \qquad (4)$$

The width $2x_m$ is at least twice the beam waist $\Delta x \approx 1.22\lambda/\mathrm{NA}_{IO}$, that is, $2x_m > 2\Delta x$, and is indicated by the shaded area in Fig. 2. This area comprises a large amount of scattered light, which determines the magnitude of $\hat{s}(z)$.

## Results

To demonstrate the degree of self-reconstruction in inhomogeneous media, we have compared a conventional Gaussian beam to a self-reconstructing Bessel beam $h_{ill}(\mathbf{r})$ applied to exactly the same refractive index distribution $n(\mathbf{r}) = n_0 + \Delta n(\mathbf{r})$ and fluorescence distribution $C(\mathbf{r}) = C_0{\cdot}(1 - \Delta n(\mathbf{r})/\Delta n_{max})$. In all experiments, non-fluorescing objects were embedded in a fluorescing gel to visualize the spread of the illumination intensity $h_{ill}(x,z)$. The angular spectrum of the Bessel beam has an annular shape with outer radius $\mathrm{NA}_{IO}{\cdot}k$ and a ring thickness $\Delta k = \mathrm{NA}_{IO}{\cdot}k{\cdot}(1 - \sqrt{\varepsilon})$ with ring aperture ratio $\varepsilon = 0.8$–$0.95$. The depths of field $\Delta z$ of the beams were adjusted by focusing the Bessel beam with a numerical aperture of the IO of $\mathrm{NA}_{IO} \approx 0.2$ and the Gaussian beam with $\mathrm{NA}_{IO} \approx 0.1$. The beams were continuously displaced along $x$ in small steps, so that distance $b$ was varied in the lateral $x$-direction relative to the centre of the image or to the scatterers at $x = 0$, respectively.

**Self-reconstruction behind large scatterers.** The first, well-defined class of refractive index inhomogeneity was represented by two large glass spheres of diameter $2a = 8\,\mu m$, which were located in a fluorescing gel cylinder at a distance $L = 19\,\mu m$ along the optical axis. Unlike the situation in previous studies[6], these particles did not block the beam, but scattered and redirected the whole beam or parts of it. How much relative energy a scatterer removes from the beam depends on its position $\mathbf{b}$ relative to the beam axis and on its size and refractive index, which is characterized by the scattering cross-section $C_{sca}$. The arrangements for self-reconstruction behind the two glass spheres were measured and simulated.

First, the illumination intensity $h_{ill}(\mathbf{r})$ was computed using a vectorial beam propagation method (BPM)[15] for both a Gaussian beam and a Bessel beam. The results are shown in Fig. 2 for the case where

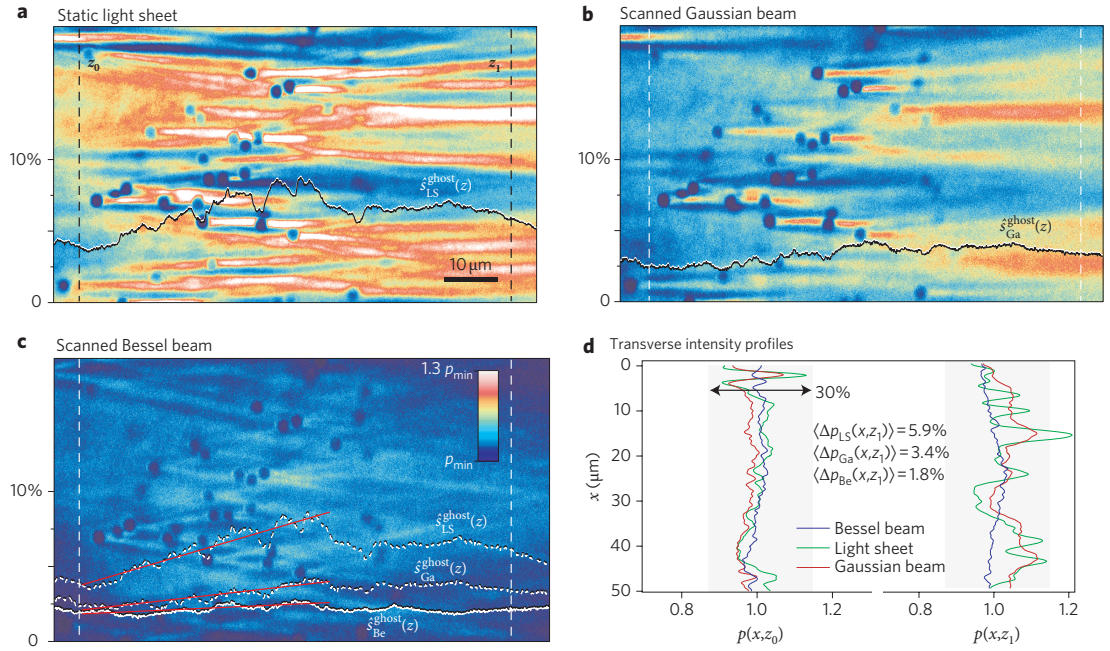


**Figure 4 | Images of a cluster of glass spheres. a–c**, Three different beam types, propagating from left to the right, illuminate non-fluorescing spheres (diameter $2a = 2$ μm) in a fluorescing gel, yielding images $p(x,z)$: a static light sheet (LS) formed by a cylindrical lens (**a**), a scanned Gaussian beam (**b**) and a scanned Bessel beam (**c**). The plot insets show the standard deviation $\hat{s}(z) \approx \hat{s}^{ghost}(z)$ of the increasing illumination inhomogeneity and line fits to $\hat{s}(z)$ (red lines). **d**, Transverse intensity profiles of the images in front of ($p(x,z_0)$) and behind ($p(x,z_1)$) the scatterers, indicated by dashed lines at the left and right edges of images **a–c**. $\langle \Delta p(x) \rangle$ denotes the mean intensity fluctuations. The grey shaded areas indicate the unique magnitude of the dynamic range of $30\% p_{min}$.

the two glass spheres are displaced by $b = a = 4$ μm from the beam centre in the $y$-direction. The simulation results show that the Gaussian beam (Fig. 2a,c,d) is deflected at the edge of the first sphere and penetrates the second sphere, nearly through its centre. In contrast, the Bessel beam (Fig. 2b,e,f) scatters at the edges of the first and second spheres, but does not change its propagation direction. It recovers its profile to a large degree, as shown in the cross-sectional plots in Fig. 2e,f.

In the corresponding experiments, the total intensity was imaged according to equation (2) and could be compared to the simulation because the point-spread function $h_{det}(\mathbf{r})$ is relatively small and therefore does not alter the illumination intensity much, although it blurs the rings of the Bessel beam. Images $p(x,z)$ for four different beam-to-bead distances $b = 7.0$, 4.2, 2.8 and 0 μm are displayed in Fig. 3a–d for the Gaussian beam and in Fig. 3e–h for the Bessel beam (see also Supplementary Movie). The experimental conditions in Fig. 3b,f correspond to the simulation shown in Fig. 2, where $b = a$. Four intensity linescans $\bar{I}_{ill}(z, b)$ averaged over a linewidth $2x_m = 4$ μm (equation (4)) are plotted in Fig. 3i for the Gaussian beam and in Fig. 3j for the Bessel beam. Here, a significant decay of $\bar{I}_{ill}(z, b)$ can be seen for the Gaussian beam due to scattering at the two spheres. This is further manifested by the standard deviation $\hat{s}(z)$ as defined in equation (3), for both beam types. Figure 3k reveals two 8-μm-wide peaks arising from the non-fluorescing spheres, but there is only a very small intensity deviation along $z$ for the Bessel beam, whereas $\hat{s}(z)$ strongly increases for the Gaussian beam.

**Self-reconstruction of beams in a cluster of spheres.** The second class of refractive index inhomogeneity was represented by several hundred 2-μm glass spheres, which were distributed randomly in a volume with a diameter of ~0.1 mm in a fluorescing gel. Comparable scattering situations were simulated numerically[15]. We tested three different beam types for their robustness against scatterers: a static light sheet generated by a cylindrical lens, a laterally scanned Gaussian beam and a laterally scanned Bessel beam. All beams had comparable depths of field along $z$. The fluorescence images $p(x,z)$ shown in Fig. 4a–c were acquired by averaging over all beam positions along $x$ for the two scanning beams and by a single acquisition for the static light sheet.

The static light sheet from a conventional selective plane illumination microscope (SPIM)[18] produced strong artefacts in the form of bright stripes that resulted from diffracted and focused light (Fig. 4a) Improvement can be seen for the scanned Gaussian beam[20] (Fig. 4b). However, the least aberrated image resulted from the scan with the self-reconstructing Bessel beam (Fig. 4c). As shown in Fig. 4d, lateral intensity linescans are relatively flat for all three illumination types in front of the cluster of spheres, but reveal intensity variations behind the cluster, which are very pronounced for the SPIM light sheet, smoother for the scanned Gaussian and nearly flat for the Bessel beam. Self-reconstruction is further manifested by the intensity standard deviations $\hat{s}^{ghost}(z)$, which are plotted as shaded curves from left to right through the images (Fig. 4a–c), as well as by the average slope of $\hat{s}(z)$, indicated by red line fits (Fig. 4c). The total intensity standard deviation can be separated into two terms, $\hat{s}(z) \approx \hat{s}^{ideal}(z) + \hat{s}^{ghost}(z)$ (as derived in the Supplementary Information, part II). The very small $\hat{s}^{ideal}(z)$ is produced by the unstained spheres, and defines the ideal contrast of the image. $\hat{s}^{ghost}(z)$ is produced by the stripe-like artefacts from the illumination, and should be minimized. Using the same dynamic range of $4\hat{s}^{ghost}_{LS} \approx 0.3$ in all images, the Bessel beam is again least affected by the scatterers and has the smallest and flattest $\hat{s}^{ghost}(z)$, as is clearly visible from Fig. 4a–c. The intensity fluctuations $\langle \Delta p(x,z_1) \rangle$ (s.d.) of the Gaussian beam are 1.9 times larger than those of the Bessel beam. The intensity fluctuations $\langle \Delta p(x,z_1) \rangle$ (s.d.) of the light sheet are 3.3 times larger.

**Self-reconstruction of beams in biological tissue.** The third class of refractive index inhomogeneity was represented by a piece of fresh human skin several hundred micrometres in size. The outer part of the skin consisted of the epidermis and the dermis, separated by the basal membrane. The first stiff layer of dead cells

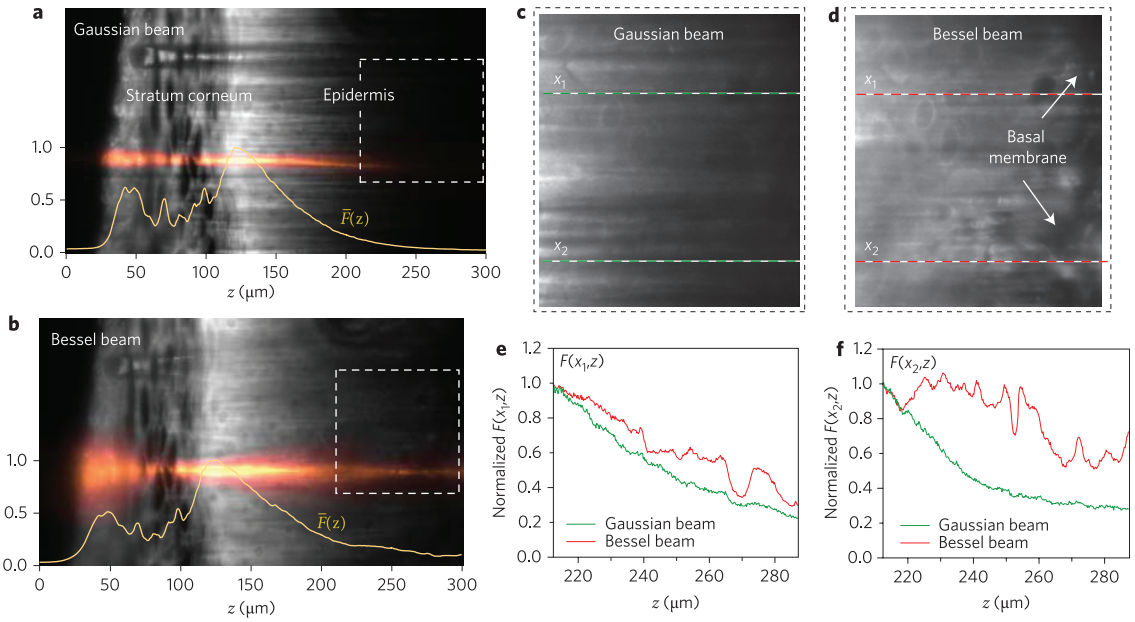


**Figure 5 | Maximum-selection images of human skin. a,b**, Illumination by a conventional beam (**a**) or a self-reconstructing beam (**b**). The beams illuminate the skin from left to right. Images from the Gaussian and Bessel beams at a single position are overlayed in orange-hot colours. Averaged intensity linescans $\overline{F}(z) \sim \overline{I}_{ill}(z)$ show an exponential decay through the epidermis. **c,d**, Part of the epidermis close to the basal membrane, magnified and autoscaled (boxes with dashed outline in **a,b**), revealing single cells only for Bessel beam illumination. **e,f**, Line scans $F(x,z)$ normalized to $F(x,z=0)$ for $x = x_1, x_2$ (indicated by dashed lines in **c,d**), showing the strong increase in contrast for the Bessel beam illumination.

in the epidermis, the stratum corneum, can be distinguished from a layer of living cells (keratinocytes), which in the following we simply refer to as the epidermis. The laser beam propagated first through the stratum corneum and then through the epidermis. Because autofluorescence was very weak, a fluorescing eosine solution was added to penetrate and stain the skin. The layers all have different, non-homogeneous refractive index distributions $n(\mathbf{r})$ and different fluorophore concentrations $C(\mathbf{r})$. A comparison between a laterally scanned Gaussian beam and a laterally scanned Bessel beam regarding their self-reconstruction ability could be performed by analysing a distance-dependent Strehl intensity ratio $SR(z)$, which is the centre-of-mass intensity of the focused beam along the propagation distance $z$ for (further details see Supplementary Information, part II). The results are shown in Fig. 5, where the propagation image of a single beam $h_{ill}(x,z,b_0)$ is overlaid in orange-hot colours on the grey-scale image of the human skin. Using identical integration times in both images, the 12-bit dynamic range of the charge-coupled device camera was fully exploited, demanding similar maximum intensities in both types of beams. For image post-processing we used the standard procedure of a maximum selection of each beam to enhance image contrast (for further details of image acquisition see Supplementary Information, part I). Again, the Gaussian beam generated more illumination artefacts in the form of stripes, and the Bessel beam enabled reduced scattering and a more homogeneous illumination without stripes. In addition, the reduced scattering of the Bessel beam at the densely packed skin cells resulted in a 55% increase in the average penetration depth $d$, as indicated by the fluorescence intensity linescans $\overline{F}(z)$ inset into the images in Fig. 5a,b. We found values of $d_{Gauss} = 50\ \mu m$ and $d_{Bessel} = 77\ \mu m$ in the epidermis ($z = 138$–$225\ \mu m$). The axial change of fluorescence intensities could be separated spatially in a region of the stratum corneum (left) and epidermis (middle), whereas the dermis (right) is hardly visible. Assuming a mean constant fluorophore concentration $\overline{C}_{epid}$ for $z > z_E$ and $\overline{C}_{strat}$ for $z < z_E$, we average $\overline{F}(z) = \overline{C}(z) \cdot \overline{I}_{ill}(z)$ over the image width $2x_m = 175\ \mu m$. The axial decay of fluorescence can be written, corresponding to equation (4), as

$$\overline{F}(z) = (2x_m)^{-1} \int_{-xm}^{xm} C(x,z) \cdot |\mathbf{E}_{tot}(x,z)|^2 dx \approx \begin{cases} \overline{C}_{strat} \cdot \overline{I}_{strat}(z) & \text{if } z < z_E \\ \overline{C}_{epid} \cdot \overline{I}_{epid}(z_E) \cdot \exp(-\overline{\rho} \cdot (\overline{\sigma}_{sca} + \overline{\sigma}_{abs}) \cdot z) & \text{if } z > z_E \end{cases} \quad (5)$$

where the illumination intensity $h_{ill}(\mathbf{r}) = |\mathbf{E}_{tot}(\mathbf{r})|^2$ separates into a field $\mathbf{E}_{tot}(\mathbf{r})$ with an average and a fluctuating phase $\overline{\phi}(\mathbf{r}) + \delta\phi(\mathbf{r})$ (for further explanations see Supplementary Information, part III). With increasing $z \gg z_E$ the number of diffusive photons increase and the correlation of their phases decreases in the epidermis. In other words, the root-mean-square (r.m.s.) deviation of the phase $\delta\phi(z) = \sqrt{-\ln(\overline{F}(z)/\overline{F}_0)}$ grows, while the intensity $\overline{F}(z) \sim \overline{I}_{ill}(z)$ along the beam axis, that is, the number of non-scattered, ballistic photons, falls off approximately exponentially. This is indicated by the second line of equation (5), which is a heuristic expression. The intensity $\overline{F}(z)$ increases at the beginning of the epidermis at $z_E \approx 120\ \mu m$ due to a higher fluorophore concentration $\overline{C}_{epid} > \overline{C}_{strat}$. For $z > z_E$, the imaged fluorescence $\overline{C}_{epid} \cdot \overline{I}_{epid}(z)$ reveals a weak exponential decay through the epidermis with decay constant $(\overline{\sigma}_{sca} + \overline{\sigma}_{abs})$. Because the mean density $\overline{\rho}$ of scatterers and the mean absorption cross-section $\overline{\sigma}_{abs}$ are the same for both beams, the mean scattering cross-section $\overline{\sigma}_{sca} \gg \overline{\sigma}_{abs}$, which should be called an effective scattering cross-section, is significantly reduced for the Bessel beam. In other words, the incident holographically shaped field $\mathbf{E}_{holo}$ determines the effective scattering cross-section and the penetration depth in dense media. This is indeed a remarkable result. Although suggested by earlier studies[23], the strength of this effect has been unexpected. This effect is further manifested by the magnified and autoscaled image areas and linescans of Fig. 5, which reveal structures on a single-cell level with the self-reconstructing Bessel beam, structures that are invisible with a Gaussian illumination beam.

## Discussion

We showed, using three different classes of refractive index inhomogeneity, that beam self-reconstruction is effective in inhomogeneous media. Through this effect it is possible to construct a new type of microscope, using self-reconstructing beams, a technique that we call MISERB. In this study the aim was to minimize scattering artefacts by using holographically shaped beams, not to optimize the image contrast.

Why is a Bessel beam less affected by scatterers than a conventional beam such as a Gaussian beam? Or, in other words, why does the perturbed beam resemble to a greater extent the unperturbed beam as expressed by equation (3)? At this point one should recall that a Gaussian beam transports about 85% of its energy within its $1/e^2$ waist with radius $R \approx 0.6\lambda/\mathrm{NA_{IO}}$, whereas our modified Bessel beam transports only about 20% of its total energy in its central lobe. The remaining energy is transported in a delocalized manner; that is, energy is transported continuously from the rings to the beam centre and therefore serves to reconstruct the beam to its initial profile. However, this energy transport is perturbed differently in the three classes of index inhomogeneity.

For the two big spheres, the most conspicuous case occurs when both beams are shifted by a distance $b =$ sphere radius $a$. Here, nearly 50% of the Gaussian field hits the sphere under a small angle and is scattered at the interface; the other half of the beam is nearly unaffected. The scattered field interferes with the unscattered field, which leads to constructive interference along the direction of beam deflection and to field extinction along the optical axis. In the Bessel beam, only a small energy fraction is conically deflected by the spheres, and the remaining energy from the rings interferes constructively without being perturbed along the optical axis. The energy decay along $z$ at the position of the first arrow in Fig. 3c,g is ~40% for the Gaussian beam (Fig. 3a,c,i), but only 5% for the Bessel beam (Fig. 3e,g,j).

In the case of the cluster of 2-μm spheres, the conventional light sheet illumination field scatters such that field amplitudes add coherently, resulting in pronounced stripes and illumination artefacts (Fig. 4). Beam scanning, on the other hand, results in an incoherent addition of scattered light, such that the energy is symmetrically scattered due to symmetric beam displacements $b$ relative to the scatterer. However, the main part of the Gaussian beam energy is effectively scattered by the spheres in the forward direction. These diffraction effects result in stripes, that is, a pronounced ghost image, which adds to the ideal image. The Bessel beam has a large cross-section relative to the 2-μm spheres, which means that although more spheres scatter, less energy is effectively taken out of the beam than for the case of the Gaussian beam. The Bessel beam scatters light in cones with angles $\sin\alpha = \mathrm{NA_{IO}}/1.33$, generating an equally distributed haze, that is, a minimized ghost image superimposed on the ideal image.

Human skin, which is a densely packed compound of different cell types, locally shifts the phase of the incident wave, resulting in r.m.s. phase deviations $\delta\phi(x,y,z)$ that increase with $z$. Because the cross-section of the Gaussian beam is less than a cell diameter, the deflection effect is similar to that of the 8-μm glass beads, although the refractive index change is much smaller. However, the slight deflection is repeated hundreds of times, which leads to beam spreading or even deflection of the Gaussian beam, resulting in a reduced penetration depth. In other words, the averaged phase fluctuations of the propagating wave are significantly larger for a Gaussian beam than for a Bessel beam. This results in an increase of more than 50% in the penetration depth into human epidermis skin of the Bessel beam relative to the Gaussian beam. This means that self-reconstruction in, and penetration through, thick media can be steered by the phase of the incident beam, that is, by a computer hologram. This unexpected result will hopefully enable new insights in medical and biological research.

In summary, Bessel beams have clearly proven their self-reconstruction ability in inhomogeneous media, and the near future will show what other types of self-reconstructing beams are useful for microscopy illumination of strongly scattering media. Another interesting challenge will be to reduce the negative influence of the Bessel rings on image contrast while maintaining their ability to transport beam-healing energy.

Received 18 March 2010; accepted 20 July 2010;
published online 12 September 2010

## References

1. Lit, J. W. Y. & Tremblay, R. Focal depth of a transmitting axicon. *J. Opt. Soc. Am.* **63,** 445–449 (1973).
2. Welford, W. T. Use of annular apertures to increase focal depth. *J. Opt. Soc. Am.* **50,** 749–753 (1960).
3. Sheppard, C. J. R. & Wilson, T. Depth of field in scanning microscope. *Opt. Lett.* **3,** 115–117 (1978).
4. Durnin, J., Miceli, J. J. & Eberly, J. H. Diffraction-free beams. *Phys. Rev. Lett.* **58,** 1499–1501 (1987).
5. Bouchal, Z., Wagner, J. & Chlup, M. Self-reconstruction of a distorted nondiffracting beam. *Opt. Commun.* **151,** 207–211 (1998).
6. Bouchal, Z. Resistance of nondiffracting vortex beam against amplitude and phase perturbations. *Opt. Commun.* **210,** 155–164 (2002).
7. Anguiano-Morales, M., Mendez-Otero, M. M., Iturbe-Castillo, M. D. & Chavez-Cerda, S. Conical dynamics of Bessel beams. *Opt. Eng.* **46,** 078001 (2007).
8. Broky, J., Siviloglou, G. A., Dogariu, A. & Christodoulides, D. N. Self-healing properties of optical Airy beams. *Opt. Express* **16,** 12880–12891 (2008).
9. Tao, S. H. & Yuan, X. C. Self-reconstruction property of fractional Bessel beams. *J. Opt. Soc. Am. A* **21,** 1192–1197 (2004).
10. Chong, A., Renninger, W. H., Christodoulides, D. N. & Wise, F. W. Airy–Bessel wave packets as versatile linear light bullets. *Nature Photon.* **4,** 103–106 (2010).
11. Dubietis, A. *et al.* Axial emission and spectral broadening in self-focusing of femtosecond Bessel beams. *Opt. Express* **15,** 4168–4175 (2007).
12. Garces-Chavez, V., McGloin, D., Melville, H., Sibbett, W. & Dholakia, K. Simultaneous micromanipulation in multiple planes using a self-reconstructing light beam. *Nature* **419,** 145–147 (2002).
13. Tuchin, V. *Tissue Optics* (SPIE Press, 2007).
14. Torok, P., Hewlett, S. J. & Varga, P. The role of specimen-induced spherical aberration in confocal microscopy. *J. Microsc.* **188,** 158–172 (1997).
15. Rohrbach, A. Artifacts resulting from imaging in scattering media: a theoretical prediction. *Opt. Lett.* **34,** 3041–3043 (2009).
16. Dodt, H. U. *et al.* Ultramicroscopy: three-dimensional visualization of neuronal networks in the whole mouse brain. *Nature Meth.* **4,** 331–336 (2007).
17. Huisken, J. & Stainier, D. Y. R. Even fluorescence excitation by multidirectional selective plane illumination microscopy (mSPIM). *Opt. Lett.* **32,** 2608–2610 (2007).
18. Huisken, J., Swoger, J., Del Bene, F., Wittbrodt, J. & Stelzer, E. H. K. Optical sectioning deep inside live embryos by selective plane illumination microscopy. *Science* **305,** 1007–1009 (2004).
19. Voie, A. H., Burns, D. H. & Spelman, F. A. Orthogonal-plane fluorescence optical sectioning—3-dimensional imaging of macroscopic biological specimens. *J. Microsc.* **170,** 229–236 (1993).
20. Keller, P. J., Schmidt, A. D., Wittbrodt, J. & Stelzer, E. H. K. Reconstruction of zebrafish early embryonic development by scanned light sheet microscopy. *Science* **322,** 1065–1069 (2008).
21. Buytaert, J. A. N. & Dirckx, J. J. J. Tomographic imaging of macroscopic biomedical objects in high resolution and three dimensions using orthogonal-plane fluorescence optical sectioning. *Appl. Opt.* **48,** 941–948 (2009).
22. Holekamp, T. F., Turaga, D. & Holy, T. E. Fast three-dimensional fluorescence imaging of activity in neural populations by objective-coupled planar illumination microscopy. *Neuron* **57,** 661–672 (2008).
23. Colak, S., Yeh, C. & Casperson, L. W. Scattering of focused beams by tenuous particles. *Appl. Opt.* **18,** 294–302 (1979).

## Acknowledgements

The authors thank Carl Zeiss MicroImaging GmbH (Jena, Germany) for support in instrument development. Further thanks go to Dr. M. Peschen and Dr. R. Pfister for providing fresh human skin as well as to Prof. Olaf Ronneberger, B. Bosworth, C. Gohn-Kreuz and P. v. Olshausen for helpful discussions. This study was supported by the Excellence Initiative of the German Federal and State Governments (EXC 294).

## Author contributions

F.F. designed the system, performed experiments and simulations, analysed the data and prepared all graphs. P.S. performed experiments on human skin. A.R. initiated and supervised the project, developed the theory and wrote the manuscript.

## Additional information

The authors declare no competing financial interests. Supplementary information accompanies this paper at www.nature.com/naturephotonics. Reprints and permission information is available online at http://npg.nature.com/reprintsandpermissions/. Correspondence and requests for materials should be addressed to F.O.F. and A.R.